Filling-driven Mott transition in SU(N) Hubbard models

Seung-Sup B. Lee, Jan von Delft, and Andreas Weichselbaum

Physics Department, Arnold Sommerfeld Center for Theoretical Physics and Center for NanoScience, Ludwig-Maximilians-Universität München, Theresienstraße 37, 80333 München, Germany

We study the filling-driven Mott transition involving the metallic and paramagnetic insulating phases in SU(N) Fermi-Hubbard models, using the dynamical mean-field theory and the numerical renormalization group as its impurity solver. The compressibility shows a striking temperature dependence: near the critical end-point temperature, it is strongly enhanced in the metallic phase close to the insulating phase. We demonstrate that this compressibility enhancement is associated with the thermal suppression of the quasiparticle peak in the local spectral functions. We also explain that the asymmetric shape of the quasiparticle peak originates from the asymmetry in the dynamics of the generalized doublons and holons.

I. INTRODUCTION

The Mott insulator transition [1], as a ubiquitous phenomenon in strongly correlated systems, appears at the boundary of various phases. One important example is the transition between metal and paramagnetic insulator in the Fermi-Hubbard model, where no symmetry (e.g., spin, discrete translational invariance) is broken across the transition. Indeed, this paramagnetic Mott transition originates purely from the competition between Coulomb interaction and kinetic energy where Mott insulators allow only integer number of particles at each site, without charge fluctuations, away from completely empty or full occupation.

Consequently, the paramagnetic Mott transition can be induced by changing the chemical potential, i.e., the filling [2–14]. This filling-driven Mott transition has been studied in realizations of the Hubbard models using ultracold atoms [15–19], in which a harmonic confinement potential is applied to the optical lattice to impose a lattice boundary. As the confinement potential is not uniform, the filling of each site varies from site to site and so different phases can appear in different regions within a single trap of atoms.

However, the filling-driven paramagnetic Mott transition has not been observed yet in ultracold atom experiments, since this requires sufficiently low temperatures relative to the Fermi energy. While the paramagnetic Mott insulator has been observed at temperature of about 20% of the Fermi energy [15–19], its evolution towards a metal occurs not via a transition but a crossover at such elevated temperature. An actual transition occurs only below the critical end point temperature, which is only a few percent of the Fermi energy [20–22].

Recently, it was demonstrated that the one-band Hubbard model with flat potential profile can be cooled down to host the antiferromagnetic phase [23]. Thus one may expect that the Hubbard model with nonuniform potential also can be brought below the critical end-point temperature of the paramagnetic Mott transition. If so, how can one discriminate between the transition and the crossover by using quantities accessible in experiments where temperature is not even directly measurable?

In this work, we study compressibility as a function of particle occupation per site, which has been measured in ultracold atom experiments [18,19], in the SU(N) Hubbard model ($2 \leqslant N \leqslant 5$) with strong Coulomb interaction. We demonstrate that it exhibits distinct behaviors depending on whether the temperature T is below, above, or near the critical end-point temperature T^*. To study the paramagnetic phases of the multiflavor model for arbitrary interaction strength, filling, and temperature, we use the dynamical mean-field theory (DMFT) [24,25] and the numerical renormalization group (NRG) [26,27] as its impurity solver.

We summarize our two main results. First, the compressibility is clearly enhanced in the metallic phase close to the insulating phase, i.e., when the occupation number is slightly away from integer, near T^*. In Ref. [7], such a compressibility enhancement (denoted as divergence therein) was first predicted for the one- and two-band Hubbard models (i.e., $N = 2$ and $N = 4$, respectively) near half-filling and explained in terms of the Landau functional. In Ref. [11], the compressibility enhancement is observed for the $N = 3$ case. Here we generalize the scenario and provide a direct connection with spectral properties: a compressibility enhancement occurs near any integer occupation (except for completely empty and full occupation) for flavor-symmetric Hubbard models for general N. As temperature grows from 0 to T^*, the compressibility gets enhanced, while at the same time the quasiparticle peak of the local spectral function gets suppressed by finite temperature.

Second, the quasiparticle peak in the metallic phase close to the Mott transition is necessarily always strongly asymmetric: the peak widths on positive and negative energy sides are different. This asymmetry arises from the strong imbalance of generalized doublon and holon occupations in the slightly doped regime with strong interaction. We substantiate this argument by studying the generalized doublon and holon correlation functions as done in our previous studies [28,29] on the subpeaks at the inner edges of the Hubbard bands [30–37].

The rest of this paper is organized as follows. In Sec. II, we provide details on the Hamiltonian and the numerical methods. In Sec. III, we study the compressibility, the local spectral function, and the local correlation functions

165143-1

of generalized doublons and holons. Sec. IV offers our conclusion.

II. METHOD

A. SU(N) Hubbard model

The SU(N) Hubbard model is the Hubbard model with N flavors of fermions, which are fully symmetric, that is, Coulomb interaction strength U, hopping amplitude t, and chemical potential are independent of particle flavor ν. Its Hamiltonian is given by

$$H = \sum_i \left[\frac{U}{2} \left(\hat{n}_i - \frac{N}{2} \right)^2 - \mu \hat{n}_i \right] - t \sum_{\langle i,j \rangle, \nu} (c_{i\nu}^\dagger c_{j\nu} + \text{H.c.}),$$

(1)

where $c_{i\nu}$ annihilates a particle with flavor $\nu = 1, \ldots, N$ at lattice site i, $\hat{n}_i \equiv \sum_\nu c_{i\nu}^\dagger c_{i\nu}$ is particle number operator, $\langle i, j \rangle$ means nearest-neighbour sites, and μ is the chemical potential with offset such that $\mu = 0$ yields particle-hole symmetry. The Hamiltonian has U(1) charge and SU(N) flavor symmetry.

The SU(N) Hubbard models had been originally considered as effective descriptions of multiband strongly correlated materials (e.g., high-temperature superconductors [38,39], fullerenes [40–43]), where the SU(N) flavor symmetry is an approximation. Recently, these models were realized in ultracold atom experiments [17,19], where the SU(N) flavor symmetry is exact and N is tunable over the range $2 \leqslant N \leqslant 6$.

We take the chemical potential μ in Eq. (1) to be uniform throughout the lattice. Results for uniform systems are useful also for studying inhomogeneous systems within the context of the local density approximation (LDA). A detailed analysis [44] shows that the LDA is a good approximation in studying both the occupation number profile (real-space distribution) and the time-of-flight (momentum-space distribution) for the Hubbard model in a harmonic trap.

B. DMFT

Dynamical mean-field theory (DMFT) [24,25] has been successfully used to study the paramagnetic Mott transition, including the filling-driven transition in the SU(N) Hubbard models [2–12]. In the single-site setting of DMFT, the Hubbard model is mapped onto the single-impurity Anderson model (SIAM). There the impurity, representing a lattice site with Coulomb interaction, is coupled to a bath of noninteracting fermions, and the energy dependence of the impurity-bath hybridization function encodes correlation effects (e.g., a Mott gap) within the rest of the lattice. The self-consistent solutions of the SIAM describe *homogeneous* phases of the original lattice model.

The mapping onto the effective impurity model relies on the approximation that the self-energy is local, i.e., momentum independent, and charge or magnetic ordering is suppressed by assuming a fully frustrated lattice. This approximation of locality becomes exact in the limit of infinite coordination number of lattice $z \to \infty$ [45]. To have finite bandwidth in this limit, the hopping amplitude is scaled as $t \propto 1/\sqrt{z}$. Then the Green's function in the lattice is derived from the impurity self-energy, using the density of states $\rho_0(\omega)$ of noninteracting lattice. In this work, we consider the semielliptic choice

$\rho_0(\omega) = \frac{2}{\pi D^2} \sqrt{D^2 - \omega^2}$, where $D \equiv 2t\sqrt{z} := 1$ is the half-bandwidth, which we set as the unit of energy. Note that the Fermi energy of the noninteracting system (i.e., the energy difference between the lowest and the highest occupied single-particle states in the absence of interaction) is $D + \mu$. We also set $\hbar = k_B = 1$ throughout.

Due to this mapping, the overall feasibility as well as the accessible parameter range of DMFT depend on which method is used as impurity solver to solve the effective impurity model. Here we use the NRG as impurity solver, since it can provide the correlation functions on the real-frequency axis directly, thus avoiding the numerically ill-posed problem of having to analytically continue imaginary-frequency data to the real axis. Also, NRG is applicable to arbitrary temperature, including infinitesimally low temperature $T = 0^+$ at comparable computational cost. See Sec. II C for details of the NRG method.

C. NRG

We solve the effective SIAM by using the full-density-matrix NRG [46,47]. The bath is discretized on a logarithmic energy grid set by the coarse-graining parameter $\Lambda = 4$. The resulting discrete impurity model is mapped exactly then onto a Wilson chain with exponentially decaying hopping. By using energy scale separation, the iterative diagonalization yields a complete basis of approximate many-body eigenstates [48,49]. Here we keep up to $N_{\text{keep}} = 2500$ low-energy multiplets at each of the early iterations corresponding to large energy scales. In later iterative diagonalization steps in the strong-coupling fixed point regime, for computational efficiency, we also apply a rescaled truncation energy threshold of $E_{\text{trunc}} = 9$, which is expected to give converged results with keeping less multiplets than N_{keep} [47]. Using a complete basis of energy eigenstates, the correlation functions at the impurity are obtained in the Lehmann representation as a collection of discrete spectral weights. To recover continuous spectral functions, we broaden the discrete spectral data with appropriate broadening kernels [46,50].

To simulate the multiflavor SIAM with feasible computational cost, we exploit the $U(1)_{\text{charge}} \otimes SU(N)_{\text{flavor}}$ symmetry in the system by making use of the QSpace tensor library for general non-Abelian symmetries [47,51]. This organizes the Hilbert space in terms of SU(N) multiplets, and operates systematically at the level of reduced matrix elements, with the Clebsch-Gordan coefficients split off and dealt with separately. This allows us to efficiently perform DMFT+NRG calculations on multiflavor models with SU(N) symmetry up to $N = 5$, bearing in mind that typical multiplet sizes grow exponentially in N [51]. Furthermore, we use the adaptive broadening scheme [50] to improve the spectral resolution of correlation functions at higher energy. Specifically, we average the results over two discretization grids ($n_z = 2$), followed by an adaptive log-Gaussian broadening whose width σ is controlled by the overall prefactor $\alpha = 2$ and a lower bound $\sigma \geqslant (\ln \Lambda)/8$. At or below the energy scale of temperature T a linear broadening is further applied to smooth out artifacts at $|\omega| \lesssim T$. See Ref. [50] and the Supplemental Material of Ref. [28] for details.

Since the NRG calculation requires less computational cost for larger Λ, here we choose a rather large value $\Lambda = 4$ to

explore $O(10^4)$ data points of (N, U, T, μ) efficiently. As a tradeoff, we have limited spectral resolution at finite energies in the local correlation functions, which is only partly regained by using the so-called z-averaging procedure, standard for NRG applications [27,35], with $n_z = 2$. In particular, with $\Lambda = 4$ the discretization is too crude, e.g., to resolve the subpeaks that are known to occur at the inner Hubbard band edges [28,29,31–33]. However, such features are irrelevant to this work: The occupation number[1] $n = N \int_{-\infty}^{\infty} d\omega \, A(\omega)/(e^{\omega/T} + 1)$ is insensitive to sharp high-energy features in the local spectral function $A(\omega) \equiv A_{cc^\dagger}(\omega) = -\frac{1}{\pi} \mathrm{Im} \langle c_{i\nu} || c_{i\nu}^\dagger \rangle_\omega$. And the physical phases are rather determined by the low-energy part of $A(\omega)$, e.g., the quasiparticle peak or the Mott gap. Moreover, we expect that the doublon-holon subpeaks [28,29] are fairly suppressed in the vicinity of the Mott transition because of the strong asymmetry in the doublon-holon dynamics to be discussed below.

As a decisive check, we also computed the local spectral functions by choosing $(\Lambda, N_{\mathrm{keep}}) = (2, 5000)$ (not shown) and compared them with the curves from $(\Lambda, N_{\mathrm{keep}}) = (4, 2500)$ with the same system parameters (the $T = 0$ curves in Fig. 5). The differences between the curves from $\Lambda = 2$ and $\Lambda = 4$ are minor; the curves from $\Lambda = 2$ slightly better resolve the spectral features, but there is no qualitative difference including the existence of the subpeaks. It is because the adaptive broadening scheme improves the spectral resolution better for larger Λ [50]. On the other hand, the choice of $(\Lambda, N_{\mathrm{keep}}) = (4, 2500)$ leads to higher truncated energy threshold than $(\Lambda, N_{\mathrm{keep}}) = (2, 5000)$ does; that is, the former gives more numerically stable result, though the numerical cost of the latter is more than an order of magnitude higher.

In this work, we study the particle occupation per lattice site $n \equiv \langle \hat{n}_i \rangle$, the compressibility $\tilde{\kappa}$ [cf. Eq. (2) below], and local correlation functions $A_{XY}(\omega) \equiv -\frac{1}{\pi} \mathrm{Im} \langle X_{i\nu} || Y_{i\nu} \rangle_\omega$, which are the imaginary part of retarded time correlators of local operators X and Y acting on site i, transformed to the frequency domain. Based on the DMFT mapping onto the SIAM and the semielliptic density of states $\rho_0(\omega)$, these local properties at a lattice site are equivalent to the same properties at the impurity when the self-consistent solution of the SIAM is achieved.

D. Compressibility

The compressibility is defined as

$$\tilde{\kappa} \equiv \frac{\partial n}{\partial \mu} \equiv n^2 \kappa, \qquad (2)$$

where we only use the derivative $\tilde{\kappa}$, without rescaling, for the remainder of the paper [19]. We obtain n for a linear grid of μ with grid size $\Delta\mu = 0.05$, and compute $\tilde{\kappa}$ by numerically differentiating $n(\mu)$. Since the latter is sensitive to numerical noise, even if the curves $n(\mu)$ look smooth except at phase transition points (cf. Fig. 1), we determine the slope of $n(\mu)$

_____

[1] In the NRG, the convolution relation $n = N \int_{-\infty}^{\infty} d\omega \, A(\omega)/(e^{\omega/T} + 1)$ holds when the local spectral function $A(\omega)$ is the discrete data in the Lehmann representation before broadening, not the continuous curve as in Fig. 5. Since the linear broadening [46,50] smooths out $A(\omega)$ for $|\omega| \lesssim T$, using the broadened $A(\omega)$ can introduce an artifact to the convolution relation.
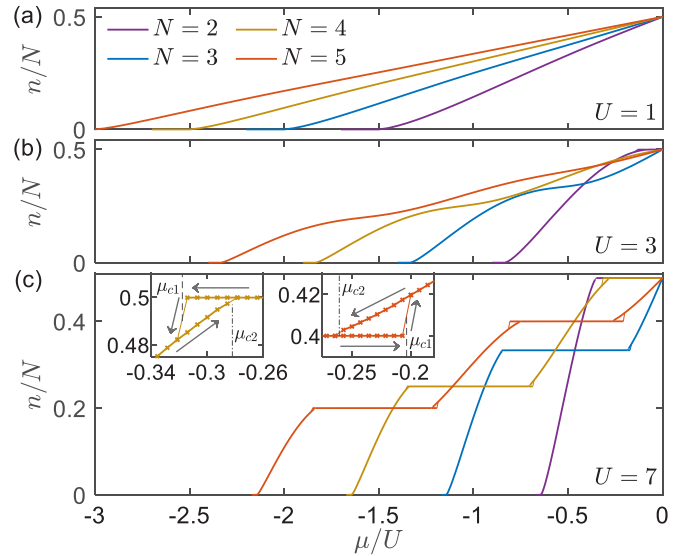

FIG. 1. Particle number per site $n \equiv \langle \hat{n}_i \rangle$ vs chemical potential μ along the homogeneous, paramagnetic phases of the SU(N) Hubbard models [cf. Eq. (1)] at temperature $T = 0$ (thick lines). Due to particle-hole symmetry at $\mu = 0$, the curves for $\mu > 0$ can be deduced by $n(\mu) = N - n(-\mu)$. (a) For small U, the systems remain compressible, i.e., metallic. (b) For intermediate $U = 3$, plateaus start to develop at integer n. (c) For large $U = 7$, wide plateaus demonstrate the incompressibility of the Mott insulating phase. As the flat plateaus for the insulating phase connect to the slanting lines for the metallic phase at the Mott transition, weak hysteretic behavior occurs, which thus indicates coexistence. Insets: Zoom-in to individual hysteresis loops for $N = 4$ and 5, as examples for the left and right ends of the Mott plateaus, respectively. Each thin solid line connects two data points (crosses) across the Mott transition: For the insulator-to-metal transition (IMT) at μ_{c1} (dashed vertical lines), it connects the last data point in a plateau with the subsequent next point in the metallic phase. Conversely, for the metal-to-insulator transition (MIT) at μ_{c2} (dash-dotted vertical lines) it connects the last point in the metallic phase (slanted line) with the next data point in the insulating plateau (here at $T = 0$, these are very short line segments visible only in the insets).

at $\mu = \mu'$ by fitting at most five consecutive points on the short interval $\mu' - 2\Delta\mu \leqslant \mu \leqslant \mu' + 2\Delta\mu$ with a quadratic polynomial. When U is larger than the critical strength, a Mott transition occurs, signaled by discontinuities in $n(\mu)$ and/or $\tilde{\kappa}(n)$, as discussed in much detail in the following sections. Thus, when μ' is close to the critical value, we exclude the points $n(\mu)$ beyond the critical value to keep the fitting error minimal.

III. RESULTS

A. Zero temperature

We start with studying the filling-driven Mott transition at $T = 0$, which by definition is free from thermal fluctuations. These results are obtained by directly solving the SIAM at infinitesimally low temperature $T = 0^+$, i.e., not by extrapolating finite-T results [9]. Indeed, this accessibility of low temperatures is a major strength of using NRG as the DMFT impurity solver [52].
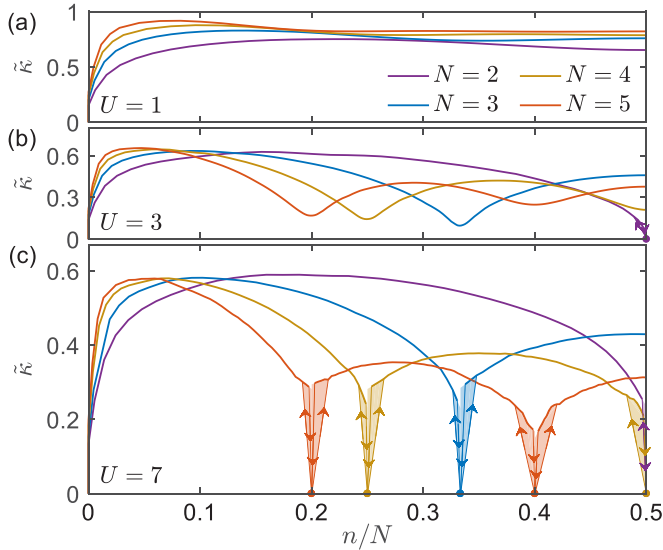
FIG. 2. Compressibility $\tilde{\kappa}$ of Eq. (2), obtained as numerical derivative from the curves in Fig. 1 at $T = 0$, as function of filling fraction n/N (thick solid lines). In (b) and (c), thin lines with arrows indicate discontinuous jumps between finite $\tilde{\kappa}$ in the metallic phase and $\tilde{\kappa} = 0$ in the insulating phases. Thus the boundary of each shaded area represents a hysteresis loop, where the upper solid line part of the boundary indicates the metallic solution in the coexistence region. Note that the shading just below $n = 1$ for $(N,U) = (2,7)$ is not visible, since the coexistence region $[\mu_{c1}, \mu_{c2}]$ in the curve $n(\mu)$ is narrower than the grid size $\Delta\mu = 0.05$. To indicate the second-order nature of MIT at $T = 0$, we have extrapolated the shaded areas to integer n, while the lines with downward arrows with finite slopes connect actual data points. The curves for $n > N/2$ can be deduced by particle-hole symmetry $\tilde{\kappa}(n) = \tilde{\kappa}(N - n)$.

In Fig. 1 we present our data on the particle number per site n vs. the full range of chemical potential μ, and in Fig. 2 we depict the corresponding compressibility $\tilde{\kappa}$ vs. filling n/N. For weak interaction $U = 1$, the compressibility $\tilde{\kappa}$ is almost independent of n for $n/N \gtrsim 0.1$. In contrast, $\tilde{\kappa}(n)$ has local minima at integer n for larger $U \gtrsim 3$. In Fig. 1, lines $n(\mu)$ with finite slope (i.e., $\tilde{\kappa} > 0$) correspond to metallic phases. Conversely, horizontal plateaus represent the incompressible phase of a Mott insulator. These plateaus appear due to an interaction-driven Mott transition, i.e., by increasing U beyond a critical interaction strength $U_c(N, [n])$ that depends on both the number of flavors N [53–55] as well as the integer filling $[n]$ of the Mott plateau [4].

At each end of a plateau in the $n(\mu)$ curves (except for $n = 0, N$), a Mott transition occurs, accompanied with a hysteresis loop [7,9], as shown in the insets of Fig. 1(c). For each hysteresis loop, we can define a pair of critical values μ_{c1} and μ_{c2} of the chemical potential: μ_{c1} is the value of the chemical potential at the outer edge of a plateau in $n(\mu)$, which thus describes an insulator-to-metal transition (IMT). Similarly, μ_{c2} is the value where the metallic solution terminates within a Mott plateau, and thus describes a metal-to-insulator transition (MIT). Therefore, in between two critical values ($\mu_{c1} < \mu < \mu_{c2}$ and $\mu_{c2} < \mu < \mu_{c1}$ for the left and right ends of the Mott plateau, respectively), both insulating and metallic phases coexist, i.e., $n(\mu)$ is double valued.

The compressibility $\tilde{\kappa}$ vs. n also shows discontinuities at integer n, associated with the Mott transition, as can be observed in Figs. 2(b) and 2(c). An IMT, depicted by an upward arrow, involve not only a jump in $\tilde{\kappa}$ but also in the occupation n. Similarly, also across a MIT, depicted by a downward arrow, a jump in both $\tilde{\kappa}$ and n could occur. However, at $T = 0$, the jump in n should disappear, such that n evolves *continuously* across MIT [9]. Thus the downward arrows in Fig. 2 should in principle be strictly vertical; the reason why they are slanted, instead, is the nonzero grid size, $\Delta\mu = 0.05$, used for our calculations.

The continuity of n and the discontinuity of $\tilde{\kappa}$ across the metal-to-insulator transition reflect the second-order nature of the Mott transition at $T = 0$. Within the coexistence regime, there exists another critical value of chemical potential μ_c at which the metallic and insulating solutions have the same values of free energy. For finite temperature $0 < T < T^*$, the transition at $\mu = \mu_c$ is first order. In contrast, for $T = 0$, one has $\mu_c = \mu_{c2} \neq \mu_{c1}$ and the transition at $\mu = \mu_c$ turns into a second-order transition [7,9], in that n is continuous but $\tilde{\kappa}$ is discontinuous (note that n and $\tilde{\kappa}$ are proportional to, respectively, the first and second derivatives of the free energy with respect to chemical potential [9]). Another exceptional situation for which the transition at $\mu = \mu_c$ is not first order arises at the critical end point $T = T^*$, where the coexistence region shrinks to a point, i.e., $\mu_c = \mu_{c1} = \mu_{c2}$, and, again, the transition becomes second order.

For $n = 0$ and $n = N$ the system is a band insulator, and thus no longer a Mott insulator. Correspondingly, we also observe no phase coexistence near the plateaus for $n = 0$ and N. Therefore while these trivial phases are still incompressible, their plateaus are excluded from our discussion of Mott plateaus. The value for the chemical potential below which the system at $T = 0$ becomes empty, is given by $\mu \leqslant \mu_0 \equiv -(N-1)\frac{U}{2} - D$, in agreement with the overall trend seen in Fig. 1. This value can be motivated as follows: By substituting $\mu' = -(N-1)\frac{U}{2}$ to μ, the first term in Eq. (1) favors zero and one occupation numbers equally. By adding another shift in the chemical potential, $\mu'' = -D$, when associated with the second term in Eq. (1), this empties this noninteracting kinetic part of the Hamiltonian. Therefore the system becomes empty ($n = 0$) for $\mu \leqslant \mu_0 \equiv \mu' + \mu''$, resulting in the above expression. Similarly, by particle-hole transformation, the system becomes completely filled ($n = N$) for $\mu \geqslant -\mu_0$.

B. Finite T and compressibility enhancement

Next we analyze the effect of finite temperature T on the compressibility curves $\tilde{\kappa}(n)$, as shown in Fig. 3. We observe that the jumps in $\tilde{\kappa}(n)$ near integer n survive for temperatures below a critical value T^*, and disappear above it. That is, T^* is the critical end point temperature of the paramagnetic Mott transition, and it depends on N, U, and n. The values of T^* for different N, n and for fixed $U = 7$ are shown in Table I. As a general trend, T^* is larger for larger N and for n closer to half-filling $N/2$. The N dependence of T^* is consistent with the result of Ref. [22], which implies that it should be easier for larger N to observe the paramagnetic Mott transition in ultracold atom systems.
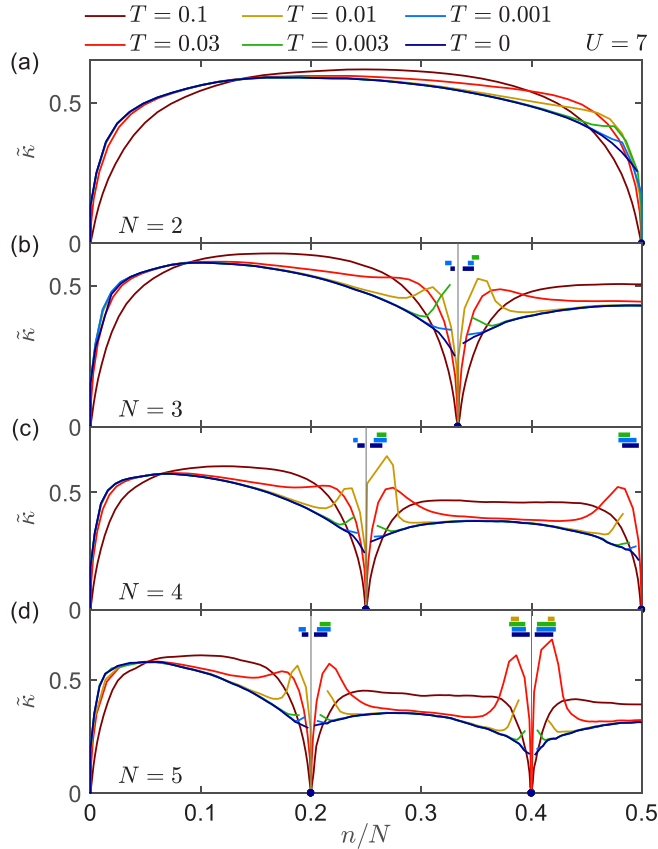
TABLE I. The critical end-point temperatures T^* of the filling-driven Mott transitions for $U = 7$. The second column of the occupation number $n = m^{+(-)}$ indicates the transition between the insulating phase with integer occupation m and the metallic phase whose occupation is larger (smaller) than m. Here T^* is estimated as the temperature above which the hysteresis loop disappears. By symmetry, it holds that $T^*(m^\pm) = T^*[(N-m)^\mp]$. The uncertainty of T^* originates from finite grid size for choosing (μ, T) and finite tolerance for the self-consistency of the DMFT.

N	n	$T^*(U = 7)$
2	1^-	0.0008(1)
3	1^-	0.004(1)
	1^+	0.005(1)
4	1^-	0.004(1)
	1^+	0.010(1)
	2^-	0.014(1)
5	1^-	0.005(1)
	1^+	0.014(1)
	2^-	0.021(1)
	2^+	0.025(1)

larger than $\lfloor N/2 \rfloor$, i.e., the down-rounded value of $N/2$. As T increases from 0 to T^*, one edge of the coexistence region, μ_{c2} for MIT, rapidly shifts towards the other edge, μ_{c1} for IMT, while μ_{c1} likewise shifts outward, but slower than μ_{c2}

FIG. 3. Compressibility $\tilde{\kappa}$ vs filling fraction n/N for fixed $U = 7$ and varying T. Below the critical end point temperature $T^*(N, U, n)$, there are Mott transitions appearing as discontinuous jumps in $\tilde{\kappa}$. Thick horizontal bars above the curves $\tilde{\kappa}(n)$ (solid lines) near integer n (vertical gray lines) indicate the range of n for the metallic phase in the coexistence regime, color matched with the curves $\tilde{\kappa}$ for the same T. As T increases from 0 to T^*, the coexistence regions get narrower in n. For some curves, e.g., for $N = 2$, the coexistence region is narrower than the numerical grid size $\Delta\mu = 0.05$. For $T \sim T^*$, local maxima of $\tilde{\kappa}(n)$ appear near integer n, which we call compressibility enhancement. At $T > T^*$, the discontinuity in the curves $\tilde{\kappa}(n)$ disappears, which indicates that a crossover (rather than a phase transition) occurs between metallic and insulating behavior.

Near and across the critical end-point temperature, $T \sim T^*$, we observe a *compressibility enhancement*: $\tilde{\kappa}(n)$ exhibits local maxima for n close, but not equal to, integer values. These local maxima of $\tilde{\kappa}(n)$ become more pronounced as T gets closer to T^*, both from above and below. For example, for the curves of $N = 5$ and $T \in [0.01, 0.03]$, a peak of $\tilde{\kappa}(n)$ associated with the compressibility enhancement is even the global maximum, not only a local maximum. In contrast, for $T = 0$ and $T = 0.1$, which are far below and above T^*, respectively, the curves $\tilde{\kappa}(n)$ decrease monotonically as n approaches an integer both from above or below, and reach zero either by a jump for $T < T^*$ or continuously for $T > T^*$.

The compressibility enhancement directly originates, by definition, from qualitative changes in the curves $n(\mu)$ for different T. In Fig. 4, we plot $n(\mu)$ for the same choice of parameter sets (N, U, T) as in Fig. 3, but zooming in towards the coexistence region of the Mott transitions, choosing n slightly
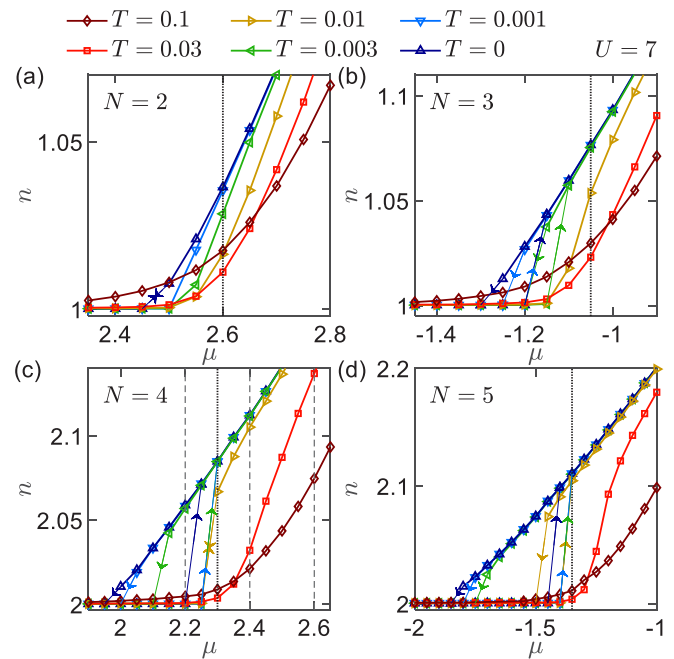

FIG. 4. Particle number per site n vs chemical potential μ zooming into the Mott transitions just above $n = \lfloor N/2 \rfloor$, i.e., particle-doped regime, for $U = 7$ and $2 \leqslant N \leqslant 5$. Thick solid lines and symbols represent $n(\mu)$. Thin lines connect data points in different phases, where the arrow specifies the direction of phase transition. For the values of μ indicated by vertical dotted lines, we show the local spectral functions in Fig. 5 below. In Fig. 6, we illustrate the local spectral functions for $N = 4$, with the μ values marked by vertical dashed lines in (c).

does. Hence the width of the coexistence regime, $|\mu_{c1} - \mu_{c2}|$, decreases. In a sense, therefore, finite temperature destabilizes the metallicity, but stabilizes the insulating phase. Interestingly, this behavior is similar to the T dependence of U_{c2} and U_{c1} at half-filling [21,55]. At the same time, the slope of the slanted part of $n(\mu)$ (corresponding to the metallic phase) in the close vicinity to integer n increases, leading to the compressibility enhancement in Fig. 3. We also see that contrary to the $T = 0$ case, not only $\tilde{\kappa}$ but also n exhibits a jump at $\mu = \mu_{c2}$ for $0 < T < T^*$.

Finally let us emphasize that while the data in Fig. 4 focuses on the particle-doped case (with n slightly above $\lfloor N/2 \rfloor$), the overall behavior for the hole-doped case (n slightly below $\lfloor N/2 \rfloor$) is completely analogous, bearing in mind that, via particle-hole transformation, one has $n(\mu) = N - n(-\mu)$.

C. Local spectral functions

The coexistence region analyzed in Fig. 4 is intricately linked to a competition between the metallicity that permits noninteger occupation, and the Mottness that constrains n to be integer. Therefore in order to gain a better understanding, we now look into the local spectral functions in the metallic regime, with a focus on the mutual interplay between average local occupation n and the quasiparticle peak in the spectral data.

The decrease of the average local occupation n towards the Mott plateau $[n]$ (the rounded value of n) as T is increased, as shown in Fig. 4, is necessarily connected to the thermal suppression of the quasiparticle peak in the local spectral function $A(\omega)$. Since its total weight, $\int_{-\infty}^{\infty} d\omega\, A(\omega) = 1$, is preserved by a sum rule, the ensuing transfer of spectral weight necessarily also influences the local occupation, $n = N \int_{-\infty}^{\infty} d\omega\, A(\omega)/(e^{\omega/T} + 1)$.

A detailed analysis of the spectral data in the metallic phase is presented in Fig. 5. There we show in each panel the local spectral functions for fixed N and μ but for several values of T. Because of the large $U = 7$, there are two well-developed Hubbard bands, centered at $\omega \sim D - U$ and $\omega \sim D$, respectively. Since μ is chosen as a fixed value slightly larger than the critical values μ_{c2} for different T, the spectral data is strongly asymmetric around $\omega = 0$ despite, e.g., $n \approx N/2$ for even N. Specifically, the lower Hubbard band (LHB) is well separated towards negative frequencies, whereas the lower edge of the upper Hubbard band (UHB) is close to the Fermi level.

In addition to the Hubbard bands, the spectral functions in Fig. 5 for $T = 0$ feature a quasiparticle peak at the Fermi level $\omega = 0$. As T increases, the quasiparticle peak gets suppressed and the occupation number n approaches $[n]$ (see middle insets). The quasiparticle peaks represent Fermi-liquid quasiparticles which, due to the narrowness of the peak, have heavy effective mass. This Fermi-liquid state hosts low-energy charge fluctuations, so noninteger n is generally possible [28].

On the other hand, for $T \geqslant 0.03 > T^*$, the significant suppression or the absence of the quasiparticle peak rules out coherent low-energy quasiparticles. So the state of the system is well described by the Hubbard bands only. If the LHB below the Fermi level is fully occupied and the UHB above the Fermi level is empty, the lattice sites are filled by an integer number of particles, $[n]$, without charge fluctuations. Accordingly, the
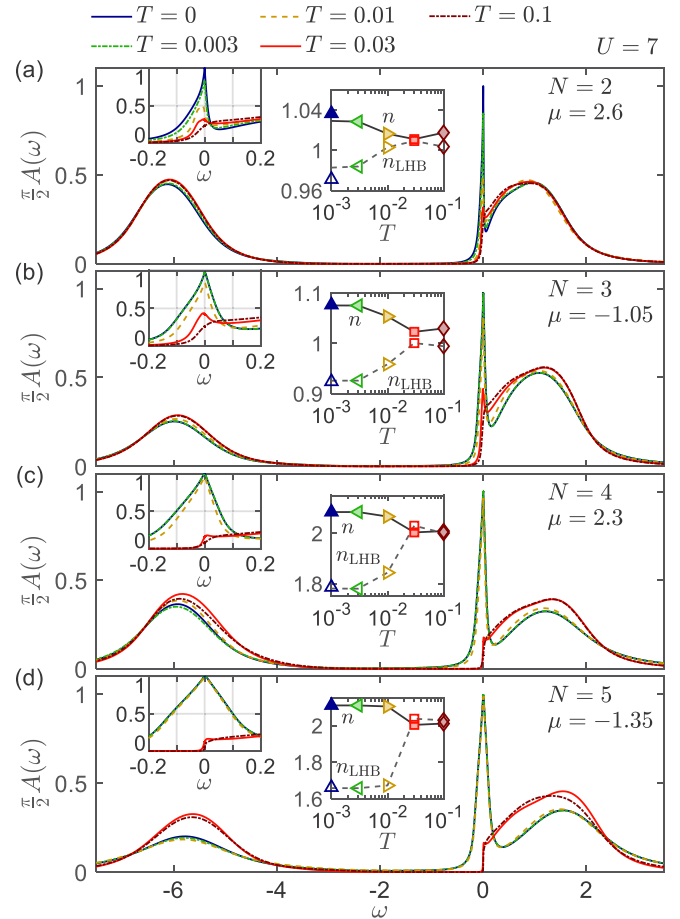

FIG. 5. Local spectral functions $A(\omega)$ in the metallic phase with slight particle doping, for large interaction $U = 7$, with varying parameters (N, T, μ), where μ corresponds to the values marked by the vertical dotted lines in Fig. 4. Left insets zoom into the low-frequency regime containing the quasiparticle peak. Middle insets show how the occupation number n (filled symbols) together with the spectral weight of the lower Hubbard band, $n_{\mathrm{LHB}} \equiv N \int_{\mathrm{LHB}} d\omega\, A(\omega)$ (empty symbols), change with T, where for the large value of U here we delineate the range of the LHB by $\omega < -2$. For reference, the dark blue symbols on top of the left axis in the middle insets give n and n_{LHB} for $T = 0$, not for $T = 10^{-3}$.

integrated spectral weights of the individual Hubbard bands would be also integers, e.g., $n_{\mathrm{LHB}} \equiv N \int_{\mathrm{LHB}} d\omega\, A(\omega) = [n]$. In Fig. 5, however where μ has been chosen slightly above μ_{c1}, the lower edge of the upper Hubbard band has dropped slightly below the Fermi level, thus making a small contribution to the occupancy. As a consequence, the values $n(T = 0.03)$ are very close to, but slightly larger than, integers $[n]$. For even larger temperature $T = 0.1$, the thermal window of the Fermi-Dirac distribution $(e^{\omega/T} + 1)^{-1}$ widens, so the occupation n deviates even more strongly from the integer $[n]$.

The T dependence of n and n_{LHB}, presented in the middle insets of Fig. 5, show how the quasiparticle weight, i.e., the spectral weight of the quasiparticle peak, is transferred to the Hubbard bands as T increases. Since the total spectral weight is preserved, the difference $[n - n_{\mathrm{LHB}}]_{T=0}$ is equivalent to the negative-frequency part of the quasiparticle weight, i.e., integrated up to $\omega = 0$. This weight is fully transferred

to the Hubbard side bands as T increases. This spectral weight transfer can be split into two net flows: the weight $[n] - n_{\text{LHB}}|_{T=0}$ is transferred to the LHB, whereas the rest, i.e., $n|_{T=0} - [n]$, together with the quasiparticle weight for $\omega > 0$, flows into the UHB. Surprisingly, despite the distance between the LHB and the Fermi level, a significant portion of the negative-frequency quasiparticle weight flows into the LHB [e.g., see the change of height in the LHB in Fig. 5(d)].

The thermal suppression of the quasiparticle peak, which is accompanied by a transfer of spectral weight, thus pushes n closer towards $[n]$ with increasing T at fixed μ. Correspondingly, $\mu_{c2}(T)$ for MIT changes much more sensitively with T than $\mu_{c1}(T)$ for IMT. In the metallic phase near $\mu_{c2}(T)$, the transfer of spectral weight from the quasiparticle peak into the LHB with increasing T necessarily leads to an increase in μ_{c2}, whereas no such weight transfer occurs near $\mu_{c1}(T)$ in the insulating phase, which lacks a quasiparticle peak. This is consistent with the fact, discussed in Sec. III B, that increasing T causes a stronger shift in $\mu_{c2}(T)$ than in $\mu_{c1}(T)$.

Once the chemical potential is outside the range of the Mott plateau (including the coexistence region), the system is always metallic, and the spectral functions evolve smoothly in terms of a crossover as temperature increases. Therefore, in this case quasiparticle peaks are present also for temperatures above T^*. This is the reason why quasiparticle peaks occur for $T = 0.03 > T^*$ in Figs. 5(a)–5(b).

However, for these high-temperature peaks the evolution with decreasing μ at fixed T is qualitatively different from those of the low-temperature peaks in the regime $T < T^*$ within the metallic phase. This is illustrated in Fig. 6, which shows how the local spectral function $A(\omega)$ evolves when μ is decreased (top to bottom) towards the MIT at μ_{c2}. As the MIT is approached while lowering μ at a given, fixed temperature, the quasiparticle peak behaves differently depending on whether that temperature lies above or below $T^* = 0.014(1)$. If the fixed temperature satisfies $T > T^*$, both the height and width of the quasiparticle peak smoothly decrease with decreasing μ, which is consistent with the crossover behavior above T^*. In contrast if the fixed temperature lies in the range $T < T^*$, the quasiparticle peak becomes narrower as μ decreases towards μ_{c2}, while its height remains almost unchanged. Once μ has passed below the MIT at μ_{c2}, the height $A(\omega = 0)$ drops abruptly, which is consistent with the transition nature below T^*. In the limiting case of $T = 0$, the spectral function $A(\omega = 0)$ is pinned to the value $2/\pi$ all along the metallic phase, as dictated by the Luttinger theorem [56]. Our DMFT+NRG result in Fig. 5 fulfills this relation with accuracy better than 3% due to the intrinsic high accuracy of NRG at low energies, despite strongly broken particle-hole symmetry. For example, at $T = 0$ the curves in Fig. 5 have the zero-frequency values $\frac{\pi}{2} A(\omega = 0) \simeq 0.9989, 0.9726, 0.9998, 0.9925$ for $N = 2, 3, 4, 5$, respectively.

Again let us emphasize that, while the spectral data in Fig. 5 above is for the particle-doped case, the spectral functions for slight hole doping can be simply deduced by particle-hole transformation, which yields the equivalence $A(\omega)|_\mu = A(-\omega)|_{-\mu}$.

We briefly discuss the effect of a nonuniform potential. In Ref. [44], the paramagnetic Mott transition of the SU(2) Hubbard model has been studied by using real-space DMFT,
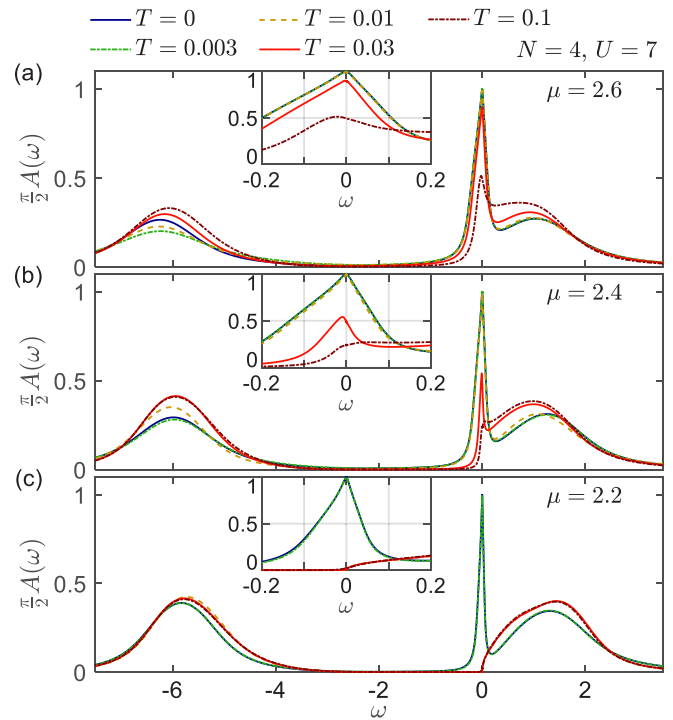

FIG. 6. Evolution of the local spectral functions $A(\omega)$ for $N = 4$, $U = 7$, and a set of five fixed temperatures, as μ is decreased (top to bottom) towards the MIT at μ_{c2}. The three μ values shown here all lie in the vicinity of the value $\mu = 2.3$ of Fig. 5(c). Insets zoom into low-frequency regime in which the quasiparticle peak or the Mott gap appears. Note that the curve for $T = 0.01$ has no quasiparticle peak in (c), since $\mu = 2.2$ lies below $\mu_{c2}(T = 0.01) = 2.275(25)$, i.e., μ has already been lowered past the MIT transition point.

which incorporates the nonuniformity of harmonic confinement potential. There the metallic phase was found to exist in a wider region than predicted by the LDA (which we imply in this work; see Sec. II A), since the metallicity can penetrate into nearby insulating regions via the Kondo effect. On the other hand, the relation between the deviation of the local occupation number from integer and the thermal suppression of the quasiparticle peak was also found there (e.g., see Fig. 5 of Ref. [44]), consistent with our result.

D. Doublon and holon correlators

The overall spectral data at finite doping as in Fig. 5, by construction, is always strongly particle-hole asymmetric. At weak doping and large U, the quasiparticle peak is necessarily close to one Hubbard band but clearly separated from the other. This asymmetry is also reflected in the shape of the quasiparticle peak itself.

It is possible to understand the origin of this asymmetry of the quasiparticle peaks by studying the correlation functions of generalized doublons and holons [28]. We define a generalized doublon (holon) as a local excitation that creates (annihilates) a particle at a lattice site filled by $[n]$ particles. Accordingly the creation operators for doublons and holons are expressed as the projected operators (so-called Hubbard operators),

$$d_{i\nu}^\dagger = c_{i\nu}^\dagger P_{i,[n]}, \quad h_{i\nu}^\dagger = c_{i\nu} P_{i,[n]}, \tag{3}$$

where $P_{i,[n]}$ is the projector onto the subspace in which site i has $[n]$ particles, and $[n]$ is the nearest integer to n. For the $N = 2$ case, the fermion operator $c_{i\nu}$ can be decomposed into doublon and holon operators, $c_{i\nu} = d_{i\nu} + h_{i\nu}^\dagger$. Thus the local spectral function can be decomposed as

$$A(\omega) = A_{dd^\dagger}(\omega) + A_{h^\dagger d^\dagger}(\omega) + A_{dh}(\omega) + A_{h^\dagger h}(\omega), \quad (4a)$$

where the relation $A_{h^\dagger d^\dagger}(\omega) = A_{dh}(\omega)$ holds generally. At the particle-hole symmetric point $\mu = 0$, we have the further relations $A_{dd^\dagger}(\omega) = A_{h^\dagger h}(-\omega)$ and $A_{dh}(\omega) = A_{dh}(-\omega)$. As before, the doublon and holon correlators for slightly hole doped cases can be deduced from the particle doping result in Fig. 7 via particle-hole symmetry:

$$A_{dd^\dagger}(\omega)|_\mu = A_{h^\dagger h}(-\omega)|_{-\mu},$$
$$A_{h^\dagger d^\dagger}(\omega)|_\mu = A_{dh}(\omega)|_\mu = A_{h^\dagger d^\dagger}(-\omega)|_{-\mu} = A_{dh}(-\omega)|_{-\mu}.$$
$$(4b)$$

For $N > 2$, the decomposition of $c_{i\nu}$ involves other projected operators, such as $c_{i\nu} P_{i,[n]-1}$, in addition to $d_{i\nu}$ and $h_{i\nu}^\dagger$. In this case, the decomposition of $A(\omega)$ in Eq. (4a) is not exact but approximate, since additional terms arise beyond those shown in Eq. (4a). However, these additional terms are negligible for large U. Indeed, the deviation $|A(\omega) - \sum_{X,Y=d,h^\dagger} A_{XY^\dagger}(\omega)|$ becomes smaller, since the probability that a site contains less than $[n] - 1$ or more than $[n] + 1$ particles is suppressed due to the large cost in Coulomb energy. Therefore the projected particle operators, which involve the projectors $P_{i,m}$ with $m > [n] + 1$ or $m < [n] - 1$ (i.e., other than doublon and holon operators) have negligible contribution to the correlation functions.

Before analyzing specific results, let us discuss a few general properties of the correlators of generalized doublons and holons. From Eq. (4a), we have three independent doublon and holon correlators, $A_{dd^\dagger}(\omega)$, $A_{dh}(\omega) = A_{h^\dagger d^\dagger}(\omega)$, and $A_{h^\dagger h}(\omega)$, as shown in Fig. 7. They reflect the overall structure of the full spectral function, including the Hubbard bands and the quasiparticle peak in the metallic phase [28]. The doublon-doublon correlator $A_{dd^\dagger}$ and the holon-holon correlator $A_{h^\dagger h}$ have two major features. $A_{dd^\dagger}$ ($A_{h^\dagger h}$) carries most of the UHB (LHB), as well as the negative (positive) frequency side of the quasiparticle peak, respectively. The latter are centered around a small energy scale $-\omega_s$ ($+\omega_s$), where a positive energy scale ω_s corresponds to the width of the quasiparticle peak centered around $\omega = 0$, which itself can be related to the energy scale of flavorlike collective modes [28] via the local dynamical flavor susceptibility. Note that, for $N = 2$, flavors equivalently represent spins for one band of electrons.

The features in the doublon-holon correlation functions necessarily correspond to dynamics at different energy scales associated with the Hubbard bands and the quasiparticle peaks, respectively. For simplicity, consider the case $N = 2$ at integer filling $n = 1$ (the generalization for different N and $[n]$ is straightforward). At $T = 0$, the positive and negative frequency sides of a correlator A_{XY} directly correspond to the Fourier transforms of $\langle X(t)Y(0)\rangle$ and $\langle X^\dagger(t)Y^\dagger(0)\rangle^*$, respectively. Hence, for example, the contribution to the UHB by $A_{dd^\dagger}$ corresponds to the dynamics of a doublon excitation added at time 0 and then again removed at time t. Conversely, the low-

energy feature centered at $\omega = -\omega_s < 0$ means that a single spin remaining after removing a doublon at time 0 undergoes a time evolution governed by the spinlike collective mode with energy scale ω_s, until a doublon is regenerated on top of the spin at time t. The features of $A_{h^\dagger h}$ can be explained analogously by swapping the roles of doublon and holon. On the other hand, the doublon-holon correlators $A_{dh}(\omega) = A_{h^\dagger d^\dagger}(\omega)$ mainly contribute to the quasiparticle peak, rather than to the Hubbard bands. It means that the doublon and holon excitations are combined at low energies to build quasiparticles.

Now we demonstrate that the asymmetry of the quasiparticle peak in Fig. 5 originates from striking differences between the generalized doublon and holon spectra, shown in Figs. 7(a)–7(d). These differences stem from the strong asymmetry in energy cost for doublon and holon excitations, due to large U, despite the low level of particle doping $(n - [n])/N < 0.03$. In the slightly particle-doped regime, the UHB (LHB) originating from local doublon (holon) excitation lies close to (far from) the Fermi level $\omega = 0$. (Note that the center-to-center distance between the LHB and the UHB is $\sim U$.) Due to this strong asymmetry, the metallic ground state in this particle-doped Mott insulator contains much more doublons than holons; correspondingly, $A_{dd^\dagger}(\omega = 0)$ is higher than $A_{h^\dagger h}(\omega = 0)$ by more than an order of magnitude. The differences in spectral strength between $A_{dd^\dagger}$ and $A_{h^\dagger h}$ in the quasiparticle peak regime, combined with the fact that the contributions of $A_{dd^\dagger}$ ($A_{h^\dagger h}$) to the quasiparticle peak are centered at $\omega = -\omega_s$ ($+\omega_s$), necessarily result in the asymmetry of the quasiparticle peak in $A(\omega)$ [cf. Eq. (4a)].

The small holon contribution to the quasiparticle peak in Figs. 7(a)–7(d) is because the LHB is far separated from the Fermi level (which originates from large U), not because the quasiparticle peaks are narrow. We consider two directions for widening the quasiparticle peaks in Figs. 7(a)–7(d): in Figs. 7(e)–7(h) we change the chemical potential to increase particle doping, while in Figs. 7(i)–7(l) we reduce the Coulomb interaction U. By increasing chemical potential μ in the first case [Figs. 7(e)–7(h)] while keeping the rest (N, U, T) the same, the systems are deeper in the metallic phase, and therefore the quasiparticle peaks become wider. With this the LHBs are even further separated from the Fermi level by the increase of μ, such that the holon-holon correlation functions $A_{h^\dagger h}$ have still negligible spectral weight in the quasiparticle regime. By decreasing U in the second case [Figs. 7(i)–7(l)], now the tails of the LHBs extend to the Fermi level. As a consequence, the quasiparticle peak also acquires a significant holon-holon contribution $A_{h^\dagger h}(\omega = 0)$, albeit still somewhat smaller as compared to the doublon-doublon contribution $A_{dd^\dagger}(\omega = 0)$.

Very small holon (doublon) contribution to the low-energy dynamics in the particle (hole)-doped system at large U is consistent with the assumption underlying the t-J model [57–61]; as an effective low-energy model for particle (hole)-doped Mott insulators, the t-J model neglects empty (doubly occupied) states of lattice sites.

IV. CONCLUSION

We have investigated the compressibility in the metallic and paramagnetic insulating phases along the filling-driven Mott
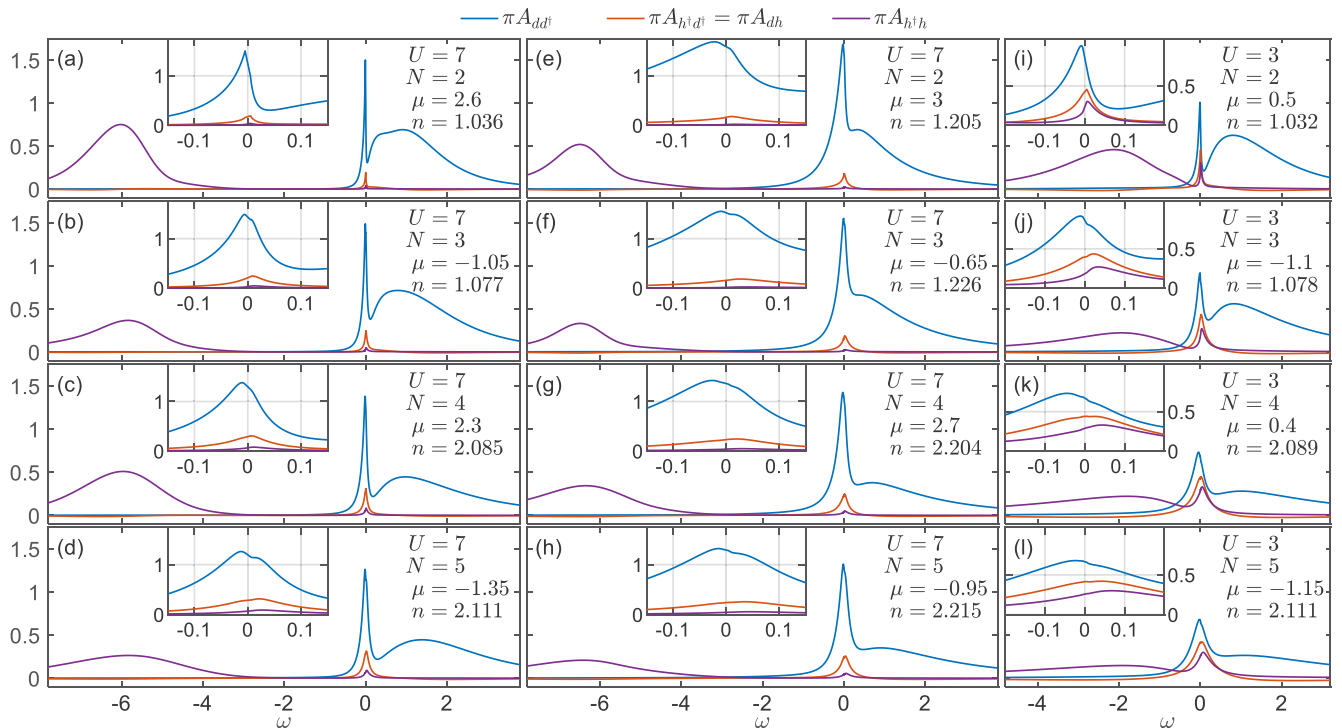
FIG. 7. The correlation functions of generalized doublons and holons at $T = 0$. The creation operators for the generalized doublons and holons, $d_{i\nu}^{\dagger}$ and $h_{i\nu}^{\dagger}$, are defined in Eq. (3). Here we choose the occupation numbers n to satisfy $[n] = \lfloor N/2 \rfloor$, where $[n]$ means the nearest integer to n. The first column of (a)–(d) show the correlation functions for the weakly particle-doped cases shown in Fig. 5. The second column [(e)–(h)] presents data for increased particle doping, whereas in the last column [(i)–(l)], the interaction strength was significantly reduced down to $U = 3$ while keeping the particle doping comparable to (a)–(d). Insets zoom into low-frequency regime containing the quasiparticle peak.

transition of the SU(N) Hubbard model. The compressibility $\tilde{\kappa}$ vs. the occupation number n exhibits distinct behaviors depending on temperature: (i) Below the critical end-point temperature T^*, $\tilde{\kappa}(n)$ discontinuously drops to zero at integer n, as the manifestation of the Mott transition. (ii) Above T^*, the curve $\tilde{\kappa}(n)$ is continuous, since the evolution between the metallic and insulating phases is now a crossover, not a phase transition. (iii) Near T^*, in the metallic phase close to the Mott insulating phase, $\tilde{\kappa}$ shows a prominent enhancement, which directly coincides with the thermal suppression of the quasiparticle peak. The quasiparticle peak represents the metallicity, in that it hosts low-energy charge fluctuations and supports noninteger occupation, while the absence of the quasiparticle peak leads to the Mottness that allows only integer occupation.

We have also shown that, in the vicinity of the filling-driven Mott transition, the asymmetric position of the Hubbard bands and the asymmetric shape of the quasiparticle peak have the same origin: different energy cost of doublon and holon excitations.

While we have focused on the paramagnetic phases in this work, magnetic ordering such as antiferromagnetism can occur in experiments, as demonstrated in Ref. [23]. It is expected that the magnetic ordering arising in the SU(N) Hubbard models would differ qualitatively depending on N [62,63]. However, such effects have not been experimentally observed yet. To describe magnetic orders, it is necessary to go beyond the single-site setting of DMFT, which we employ here, by using,

e.g., bipartite lattice setting of DMFT [22,64–66], real-space DMFT [44], or the cluster extensions of DMFT [67–72]. It would be interesting to study the compressibility in the presence of magnetic ordering, yet this is beyond the scope of this work.

For the purpose of this paper, the paramagnetic Mott transition may be achieved in ultracold atom experiments by tuning the critical temperature of the magnetic transition significantly below the paramagnetic transition. The critical temperature of the magnetic transition can be lowered by having frustration in the system, such as next-nearest-neighbour hopping or non-bipartite (e.g., triangular) lattice. Another option is to increase the number N of flavors, which increases the critical end-point temperature T^* of the paramagnetic transition [22,55] (see Table I; also see Figs. 1 and 3 in that the coexistence region gets wider with larger N), yet decreases the critical temperature for the magnetic transition (e.g., according to Ref. [22], the former becomes larger than the latter for $N \geqslant 6$). This option is appealing in that, for larger N, lower system temperatures are accessible, since the Pomeranchuk effect, a mechanism to cool down cold atoms, becomes stronger [17,19,73].

[1] M. Imada, A. Fujimori, and Y. Tokura, Rev. Mod. Phys. **70**, 1039 (1998).

[2] D. S. Fisher, G. Kotliar, and G. Moeller, Phys. Rev. B **52**, 17112 (1995).

[3] H. Kajueter, G. Kotliar, and G. Moeller, Phys. Rev. B **53**, 16214 (1996).

[4] M. J. Rozenberg, Phys. Rev. B **55**, R4855 (1997).

[5] H. Kajueter and G. Kotliar, Int. J. Mod. Phys. B **11**, 729 (1997).

[6] J. E. Han, M. Jarrell, and D. L. Cox, Phys. Rev. B **58**, R4199 (1998).

[7] G. Kotliar, S. Murthy, and M. J. Rozenberg, Phys. Rev. Lett. **89**, 046401 (2002).

[8] T. Fujiwara, S. Yamamoto, and Y. Ishii, J. Phys. Soc. Jpn. **72**, 777 (2003).

[9] P. Werner and A. J. Millis, Phys. Rev. B **75**, 085108 (2007).

[10] K. Inaba and A. Koga, J. Phys. Soc. Jpn. **76**, 094712 (2007).

[11] E. V. Gorelik and N. Blümer, Phys. Rev. A **80**, 051602 (2009).

[12] L. Del Re and M. Capone, arXiv:1708.00310.

[13] H. Hasegawa, J. Phys. Soc. Jpn. **66**, 3522 (1997).

[14] S. Onoda and M. Imada, J. Phys. Soc. Jpn. **70**, 3398 (2001).

[15] R. Jördens, N. Strohmaier, K. Gunter, H. Moritz, and T. Esslinger, Nature (London) **455**, 204 (2008).

[16] U. Schneider, L. Hackermüller, S. Will, T. Best, I. Bloch, T. A. Costi, R. W. Helmes, D. Rasch, and A. Rosch, Science **322**, 1520 (2008).

[17] S. Taie, R. Yamazaki, S. Sugawa, and Y. Takahashi, Nature Phys. **8**, 825 (2012).

[18] P. M. Duarte, R. A. Hart, T.-L. Yang, X. Liu, T. Paiva, E. Khatami, R. T. Scalettar, N. Trivedi, and R. G. Hulet, Phys. Rev. Lett. **114**, 070403 (2015).

[19] C. Hofrichter, L. Riegger, F. Scazza, M. Höfer, D. R. Fernandes, I. Bloch, and S. Fölling, Phys. Rev. X **6**, 021030 (2016).

[20] N. Blümer, Ph.D. thesis, Universität Augsburg, 2002.

[21] R. Bulla, T. A. Costi, and D. Vollhardt, Phys. Rev. B **64**, 045103 (2001).

[22] H. Yanatori and A. Koga, Phys. Rev. B **94**, 041110 (2016).

[23] A. Mazurenko, C. S. Chiu, G. Ji, M. F. Parsons, M. Kanász-Nagy, R. Schmidt, F. Grusdt, E. Demler, D. Greif, and M. Greiner, Nature (London) **545**, 462 (2017).

[24] A. Georges, G. Kotliar, W. Krauth, and M. J. Rozenberg, Rev. Mod. Phys. **68**, 13 (1996).

[25] G. Kotliar, S. Y. Savrasov, K. Haule, V. S. Oudovenko, O. Parcollet, and C. A. Marianetti, Rev. Mod. Phys. **78**, 865 (2006).

[26] K. G. Wilson, Rev. Mod. Phys. **47**, 773 (1975).

[27] R. Bulla, T. A. Costi, and T. Pruschke, Rev. Mod. Phys. **80**, 395 (2008).

[28] S.-S. B. Lee, J. von Delft, and A. Weichselbaum, Phys. Rev. Lett. **119**, 236402 (2017).

[29] S.-S. B. Lee, J. von Delft, and A. Weichselbaum, Phys. Rev. B **96**, 245106 (2017).

[30] X. Y. Zhang, M. J. Rozenberg, and G. Kotliar, Phys. Rev. Lett. **70**, 1666 (1993).

[31] M. Karski, C. Raas, and G. S. Uhrig, Phys. Rev. B **72**, 113110 (2005).

[32] M. Karski, C. Raas, and G. S. Uhrig, Phys. Rev. B **77**, 075116 (2008).

[33] M. Ganahl, P. Thunström, F. Verstraete, K. Held, and H. G. Evertz, Phys. Rev. B **90**, 045144 (2014); M. Ganahl, M. Aichhorn, H. G. Evertz, P. Thunström, K. Held, and F. Verstraete, *ibid.* **92**, 155132 (2015).

[34] F. A. Wolf, I. P. McCulloch, O. Parcollet, and U. Schollwöck, Phys. Rev. B **90**, 115124 (2014).

[35] R. Žitko and T. Pruschke, Phys. Rev. B **79**, 085106 (2009).

[36] M. Granath and H. U. R. Strand, Phys. Rev. B **86**, 115111 (2012).

[37] Y. Lu, M. Höppner, O. Gunnarsson, and M. W. Haverkort, Phys. Rev. B **90**, 085102 (2014).

[38] I. Affleck and J. B. Marston, Phys. Rev. B **37**, 3774 (1988).

[39] J. B. Marston and I. Affleck, Phys. Rev. B **39**, 11538 (1989).

[40] J. P. Lu, Phys. Rev. B **49**, 5687 (1994).

[41] O. Gunnarsson, E. Koch, and R. M. Martin, Phys. Rev. B **54**, R11026 (1996).

[42] P. Mahadevan and D. D. Sarma, Phys. Rev. B **59**, 1739 (1999).

[43] E. Koch, O. Gunnarsson, and R. M. Martin, Phys. Rev. B **60**, 15714 (1999).

[44] R. W. Helmes, T. A. Costi, and A. Rosch, Phys. Rev. Lett. **100**, 056403 (2008).

[45] W. Metzner and D. Vollhardt, Phys. Rev. Lett. **62**, 324 (1989).

[46] A. Weichselbaum and J. von Delft, Phys. Rev. Lett. **99**, 076402 (2007).

[47] A. Weichselbaum, Phys. Rev. B **86**, 245124 (2012).

[48] F. B. Anders and A. Schiller, Phys. Rev. Lett. **95**, 196801 (2005).

[49] F. B. Anders and A. Schiller, Phys. Rev. B **74**, 245113 (2006).

[50] S.-S. B. Lee and A. Weichselbaum, Phys. Rev. B **94**, 235127 (2016).

[51] A. Weichselbaum, Ann. Phys. (NY) **327**, 2972 (2012).

[52] R. Bulla, Phys. Rev. Lett. **83**, 136 (1999).

[53] Y. Ōno, M. Potthoff, and R. Bulla, Phys. Rev. B **67**, 035119 (2003).

[54] K. Inaba, A. Koga, S.-i. Suga, and N. Kawakami, Phys. Rev. B **72**, 085112 (2005).

[55] N. Blümer and E. V. Gorelik, Phys. Rev. B **87**, 085115 (2013).

[56] E. Müller-Hartmann, Z. Phys. B **76**, 211 (1989).

[57] A. B. Harris and R. V. Lange, Phys. Rev. **157**, 295 (1967).

[58] K. A. Chao, J. Spalek, and A. M. Oles, J. Phys. C **10**, L271 (1977).

[59] A. H. MacDonald, S. M. Girvin, and D. Yoshioka, Phys. Rev. B **37**, 9753 (1988).

[60] H. Eskes and A. M. Oleś, Phys. Rev. Lett. **73**, 1279 (1994).

[61] H. Eskes, A. M. Oleś, M. B. J. Meinders, and W. Stephan, Phys. Rev. B **50**, 17980 (1994).

[62] C. Honerkamp and W. Hofstetter, Phys. Rev. Lett. **92**, 170403 (2004).

[63] M. Cazalilla and A. Rey, Rep. Prog. Phys. **77**, 124401 (2014).

[64] R. Chitra and G. Kotliar, Phys. Rev. Lett. **83**, 2386 (1999).

[65] R. Zitzler, N.-H. Tong, T. Pruschke, and R. Bulla, Phys. Rev. Lett. **93**, 016406 (2004).

[66] A. Camjayi, R. Chitra, and M. J. Rozenberg, Phys. Rev. B **73**, 041103 (2006).

[67] M. Balzer, B. Kyung, D. Sénéchal, A.-M. S. Tremblay, and M. Potthoff, Europhys. Lett. **85**, 17002 (2009).

[68] E. Gull, M. Ferrero, O. Parcollet, A. Georges, and A. J. Millis, Phys. Rev. B **82**, 155101 (2010).

[69] G. Sordi, K. Haule, and A.-M. S. Tremblay, Phys. Rev. Lett. **104**, 226402 (2010).

[70] G. Sordi, K. Haule, and A.-M. S. Tremblay, Phys. Rev. B **84**, 075161 (2011).

[71] G. Sordi, P. Sémon, K. Haule, and A.-M. S. Tremblay, Phys. Rev. Lett. **108**, 216401 (2012).

[72] L. Fratino, M. Charlebois, P. Sémon, G. Sordi, and A.-M. S. Tremblay, Phys. Rev. B **96**, 241109 (2017).

[73] K. R. A. Hazzard, V. Gurarie, M. Hermele, and A. M. Rey, Phys. Rev. A **85**, 041604 (2012).